Available online at www.sciencedirect.com
ScienceDirect
Journal of Solid State Chemistry 180 (2007) 1333–1339
JOURNAL OF SOLID STATE CHEMISTRY
www.elsevier.com/locate/jssc

Synthesis, structure and properties of $Li_2Rh_3B_2$

Mark S. Bailey[a], Emil B. Lobkovsky[b], David G. Hinks[a], Helmut Claus[a], Yew San Hor[a], John A. Schlueter[a], John F. Mitchell[a,*]

[a]*Materials Science Division, Argonne National Laboratory, Argonne, IL 60439, USA*
[b]*Department of Chemistry and Chemical Biology, Cornell University, Ithaca, NY 14853, USA*

Received 6 January 2007; received in revised form 7 February 2007; accepted 12 February 2007
Available online 21 February 2007

Abstract

$Li_2Rh_3B_2$ has been synthesized at 1000 °C from a stoichiometric mix of rhodium and boron and an excess of lithium. $Li_2Rh_3B_2$ crystallizes in the orthorhombic space group *Pbam* (no. 55, $Z = 2$) with room temperature lattice constants $a = 5.7712(1)$ Å, $b = 9.4377(2)$ Å, $c = 2.8301(1)$ Å and cell volume 154.149(6) Å^3. The structure was solved from single crystal X-ray diffraction yielding the final R indices (all data) $R1 = 2.8\%$ and w$R2 = 4.7\%$. The structure is a distortion of the $CeCo_3B_2$ structure type, containing a network of Rh_6B trigonal prisms and short Li–Li contacts of 2.28(2) Å. $Li_2Rh_3B_2$ is a diamagnetic metal with a room temperature resistivity of 19 μΩ cm, as determined by magnetic susceptibility and single crystal transport measurements. The measured diamagnetism and electronic structure calculations show that $Li_2Rh_3B_2$ contains rhodium in a d^{10} configuration.
Published by Elsevier Inc.

Keywords: Metal flux; Lithium flux; Ternary lithium rhodium boride; Crystal growth

1. Introduction

There are a number of classes of boron-containing materials that exhibit superconductivity at relatively high temperatures. The most striking example is the binary material MgB_2 whose transition temperature (T_c) of 40 K is the highest so far reported for a binary system [1]. Superconductivity in ternary or higher borides is most commonly found in compounds containing the more electronegative transition elements such as ruthenium, palladium or iridium [2]. For example, the material with the nominal composition $YPd_5B_3C_x$ was reported to become superconducting below approximately 23 K [3] and the ternary compounds YRh_4B_4, $LuRuB_2$ and $LaRh_3B_2$ are examples of superconducting materials studied extensively [4] before the discovery of superconductivity in the cuprates [5]. More recently, superconductivity has been reported in the isostructural compounds Li_2Pd_3B ($T_c = 8$ K) and Li_2Pt_3B ($T_c = 2.8$ K) [6,7]. It is interesting to note that all the transition metals mentioned above are more electronegative than boron and would be expected to formally oxidize boron in compounds such as $LaRh_3B_2$ and Li_2Pt_3B.

Boron can adopt a number of different bonding motifs in the solid state. The binary borides $LiB_{\sim 0.8}$ [8], MgB_2 [9] and LaB_6 [9], exhibit boron–boron chains, planes and three-dimensional, polyhedral-based networks, respectively. Boron also adopts a variety of roles when combined with transition metals, for example, within the Cr–B phase diagram there are examples of isolated boron atoms (Cr_2B), boron chains (CrB) and boron planes (CrB_2) [10]. The structural diversity of boron so far discovered in the ternary or higher superconductors is more limited, e.g., all the materials mentioned above contain either boron trimers ($YPd_5B_3C_x$), dimers (YRh_4B_4) or isolated species (Li_2Pd_3B). In metallic borides containing isolated boron atoms, the trigonal prismatic coordination is most common, e.g., in $LaRh_3B_2$, but the structure of Li_2Pd_3B is based upon distorted BPd_6 octahedra that form an unusual vertex-connected $^{\infty}_{3}|BPd_{6/2}$ network [11]; in fact, both Li_2Pd_3B and Li_2Pt_3B are proving fascinating to the condensed matter community as they are members of a

*Corresponding author. Fax: +1 630 252 7777.
E-mail addresses: mbailey@anl.gov (M.S. Bailey), mitchell@anl.gov (J.F. Mitchell).

0022-4596/$ - see front matter Published by Elsevier Inc.
doi:10.1016/j.jssc.2007.02.006

small class of materials that exhibit superconductivity but whose structure lacks inversion symmetry [12].

Impediments to the discovery of new boron-containing materials include inherent synthetic challenges, for example, boron is a high-melting element that becomes highly reactive towards typical container materials at such elevated temperatures. High-temperature synthesis of borides is often accomplished via arc-welding on water-cooled hearths but lower temperature regimes have been explored via fluxes such as copper [13], aluminum [13], gallium [14] or Ni_2B [15]. It is apparent that the nature and composition of the flux employed affects the products afforded by given set of reagents [13].

We are interested in both discovering electronically interesting borides and in exploring the feasibility of lithium as a flux for growing novel materials. This paper reports our initial work in this area by describing the synthesis and properties of $Li_2Rh_3B_2$, a material with a close relation to the family of compounds that includes $LaRh_3B_2$ (superconductor, $T_c = 3$ K) and $CeRh_3B_2$ (ferromagnet, $T_c = 115$ K [4]). We find $Li_2Rh_3B_2$ to be a diamagnetic metal but observe no superconducting transitions above 1.3 K, an observation that allows us to speculate upon the necessary requirements for superconductivity in $LaRh_3B_2$. During the review process, it was noted by us that $Li_2Rh_3B_2$ is reported in the Ph.D. thesis of Mirgel [16] and found to be stable in air and concentrated hydrochloric acid.

2. Experimental

$Li_2Rh_3B_2$ was initially synthesized serendipitously in an attempt to prepare platinum-containing borides. Inside an argon-filled glove box, 100 mg Li (pieces from rod, surface mechanically cleaned, 99.9% Alfa Aesar), 19 mg B (chunks, 99.9999%, Eagle Picher) and 348 mg Pt wire (unknown purity) were loaded into a 3/8 in. OD niobium tube, providing the following elemental ratio 10Li:1B:1Pt. The tube was welded shut under flowing argon (99.999%, further purified by flowing over Ti metal at 800 °C) using a Centorr Associates arc furnace and subsequently sealed under vacuum in an evacuated fused silica sheath. The reaction tube was placed upright into a muffle furnace, heated to 1000 °C at 2 °C min^{-1}, held at temperature for 61 h, then cooled to room temperature at 1 °C min^{-1}. The niobium tube was opened inside the glove box and the excess lithium removed in approximately 8 h via distillation under dynamic vacuum (~5 mTorr) and a temperature gradient from 575 °C to room temperature.

Once the elemental composition of $Li_2Rh_3B_2$ was determined (*vide infra*) subsequent reactions were carried out. Three reactions were loaded that contained similar quantities to that listed above but provided the molar ratios xLi:2B:3Rh (powder, 99.95%, Aesar) with $x = 10$, 20 and 200. These reactions were performed in an identical manner to that described above except that the reaction containing 200Li:3Rh:2B was placed in dynamic vacuum at 575 °C for 11 h.

Three samples of $CaRh_3B_2$ were prepared by arc-welding. In every case, an excess of calcium was used as significant calcium loss was observed during welding. The reagents were initially pressed into a pellet that was subsequently melted three times and flipped between each melting. Reaction 1 was between 1.4Ca:3Rh:2B. Reaction 2 was between 1.4Ca:1"Rh_3B_2", where "Rh_3B_2" denotes a pre-arc-welded mixture of 3Rh:2B. Reaction 3 was between 2Ca:1"Rh_3B_2".

Single crystal X-ray diffraction was performed with a Bruker X8 Apex II Diffractometer. Suitable crystals were selected under polybutene oil and loaded onto the goniometer head via a nylon loop. Once loaded, a stream of cold nitrogen froze the crystal, keeping it both stationary and protected from the atmosphere. Data were collected and reduced with the APEX2 and SAINT-Plus software packages [17], respectively. An empirical absorption correction was applied with the program SADABS [18], and data analysis was carried out with the SHELX [19] suite of programs and WinGX [20]. Powder X-ray diffraction analysis was carried out on a PANalytical X'Pert Pro MPD in Bragg-Brentano geometry with CoKα radiation and an X'celerator detector. Samples were ground in an agate mortar inside an argon-filled glove box, loaded onto a greased sample slide and covered with Mylar film (0.00012 in. thick) before being transported to the diffractometer.

Electron microprobe analysis was carried out on a Hitachi S-2700 SEM. A sample of $Li_2Rh_3B_2$ was transferred under argon to a constantly purged nitrogen glove bag equipped with an optical microscope. Crystals of $Li_2Rh_3B_2$ were selected, placed on a carbon tape and transferred to the SEM in a nitrogen atmosphere. The sample holder was quickly transferred to the antechamber, resulting in minor but unavoidable air exposure.

All samples were initially screened for superconducting transitions using a locally built, low-field SQUID magnetometer that incorporates a double μ-metal shield to reduce the residual field to below 10^{-2} G [21]. For each measurement, approximately 10–20 mg of a sample was loaded into a hermetically sealed titanium capsule. Magnetization data were taken on warming in a field of 1 G after zero field cooling to 1.3 K.

A Quantum Design MPMS SQUID Magnetometer was used to measure the DC magnetization of a 141 mg sintered pellet of $Li_2Rh_3B_2$. The diameter of the pellet was well matched to the inside diameter of the straw used to suspend the sample inside the pick-up coils; therefore, the pellet could be loaded directly into the straw without the need for a gel cap or other sample holder. The sample was loaded into the straw inside an argon-filled glove box and transported to the SQUID in an argon atmosphere before being quickly loaded into the sample space.

A DC four-probe resistivity measurement was performed on a single crystal of $Li_2Rh_3B_2$. A sample of $Li_2Rh_3B_2$ was

transferred to the nitrogen purged glove bag, and a single crystal of rod-like habit [$(0.05 \times 0.05 \times 0.9)\,mm^3$] was fixed to a quartz coverslip with a dab of fast-setting epoxy. Four gold wires were attached to the crystal with silver epoxy, which was cured (~160 °C, 20 min) in the nitrogen purged glove bag. Once the silver epoxy had cured, the crystal and contacts were immediately encapsulated inside non-conducting fast-setting epoxy. DC resistance measurements were obtained on cooling and warming in 1 K increments between 300 and 2.3 K with a Quantum Design PPMS, using a 1 mA excitation current.

The electronic structure of $Li_2Rh_3B_2$ was calculated at the extended Hückel level with the program YAeHMOP [22] using Slater-type orbitals. Default values of orbital energies and exponents were used [23]. Average properties were calculated using a set of 216 k points within the irreducible wedge of the first Brillouin zone.

3. Results and discussion

As mentioned above, the initial reaction contained platinum wire. Following the removal of the excess lithium, the content of the niobium tube was easily removed, revealing an inhomogeneous mixture of red and silvery-gold powder. A fraction of this sample was studied under an optical microscope in a nitrogen atmosphere. The sample contained a mixture of gray metallic shards, transparent red crystals and a small fraction of rod-like crystals. Several rod-like crystals were analyzed with single crystal X-ray diffraction, all yielding reflections that could be indexed on an orthorhombic cell with lattice parameters of approximately $a = 5.77$ Å, $b = 9.401$ Å and $c = 2.82$ Å. Such a cell could not be found in our databases [24]; therefore, the most suitable crystal [$(0.02 \times 0.03 \times 0.13)\,mm^3$] was selected for data collection. The systematic absences presented as possible space groups *Pbam* (no. 55) and *Pba*2 (no.32). The heavy atoms could be located with either direct methods or via a Patterson map and identical solutions were obtained in both space groups; therefore, the solution in the higher symmetry space group (*Pbam*) was chosen and no higher symmetry was found by the program ADDSYM [20].

The optimal X-ray solution stoichiometry at this point was $Li_2Pt_3B_2$; however, the Fourier difference map clearly showed the platinum site contained too many electrons to correctly model the observed electron density. Analysis, via EDS–SEM, of crystals with the same distinctive habit detected only a signal for rhodium. The signal for lithium and boron is too weak to be observed by EDS; however, that of rhodium cannot be mistaken. We speculate that the "platinum" wire used in the reaction was actually a platinum–rhodium alloy. Rhodium was therefore placed onto the heavy metal site and the difference Fourier map immediately smoothed to acceptable values. These and other details of the crystal structure refinement can be found in Table 1. The atomic coordinates, standardized with STRUCTURE TIDY [25], and (equivalent) isotropic displacement parameters are shown in Table 2. Anisotropic displacement parameters were employed only for the rhodium atoms and the refined values are given in Ref. [26]. There was no indication for partial occupancy of any of the atomic sites from X-ray diffraction but, due to the small scattering power of Li and B, this cannot be ruled out. Further details of the crystal structure investigations are available from the Fachinformationszentrum Karlsruhe, D-76344 Eggenstein-Leopoldshafen (Germany) on quoting the depository number CSD-417442, the name of the authors and citation of this paper.

Table 1
Crystal data and structure refinement for $Li_2Rh_3B_2$

Empirical formula	$Li_2Rh_3B_2$
Formula weight ($g\,(mol)^{-1}$)	344.23
Temperature (K)	173
Wavelength	0.71073 Å
Space group/no.	*Pbam*/55
a (Å)	5.773(1)
b (Å)	9.401(2)
c (Å)	2.8217(6)
Volume (Å^3)	153.14(6)
Z	2
ρ (calculated) ($mg\,m^{-3}$)	7.465
θ range	4.14–36.42
Reflections collected/unique	2551/435 [$R_{int} = 0.0312$]
Completeness to $\theta = 36.42$	99.5%
Data/restraints/parameters	435/0/18
Goodness-of-fit on F^2	1.172
R indices [$I > 2\sigma(I)$]	$R1 = 0.0202$, w$R2 = 0.0459$
R indices (all data)	$R1 = 0.0280$, w$R2 = 0.0470$
Extinction coefficient	0.044(2)
Largest diffraction peak and hole ($e\,Å^{-3}$)	1.555 and −1.443

Table 2
Atomic coordinates and isotropic (Li and B) or equivalent isotropic (Rh) displacement parameters ($Å^2 \times 10^3$) for $Li_2Rh_3B_2$

Atom	Wyckoff	x	y	z	U(iso/eq)
B	4(h)	0.062(1)	0.1680(6)	0.5	5(1)
Li	4(h)	0.157(2)	0.426(1)	0.5	10(2)
Rh(1)	4(g)	0.3344(1)	0.2211(1)	0	3(1)
Rh(2)	2(a)	0	0	0	3(1)

The equivalent isotropic displacement parameter is defined as one-third of the trace of the orthogonalized U_{ij} tensor.

Bulk samples of $Li_2Rh_3B_2$ could be synthesized from reactions containing xLi:3Rh:2B ($x = 10$, 20, 200). Following lithium removal, the $x = 20$ reaction provided a sample that was, according to powder X-ray diffraction, phase pure: the program FULLPROF [27] was used to extract the lattice parameters $a = 5.7712(1)$ Å, $b = 9.4377(2)$ Å and $c = 2.8301(1)$ Å via a Le Bail refinement in *Pbam* from all the observed peaks. The cell volume obtained, 154.149(6) Å^3, is as expected, slightly larger (~0.8%) than that obtained at 170 K via single crystal analysis. This sample (with $x = 20$) was used for the magnetization measurements detailed below. Following lithium removal, the powder X-ray diffraction patterns of samples from

both the $x = 10$ and $x = 200$ reactions contained impurity peaks at approximately 23.8° 2θ (CoKα), consistent with LiRh. The intensity of this peak was approximately 3% that of main $Li_2Rh_3B_2$ peak when $x = 200$, but 46% of the main $Li_2Rh_3B_2$ peak when $x = 10$. In addition to the LiRh peak, a second equally intense impurity peak at ~26.9° 2θ (CoKα) that could not be assigned was observed in the $x = 10$ reaction. The $x = 200$ sample provided the largest crystals and it was from this reaction that the crystal used for transport measurements was obtained.

3.1. Structure description

The structure of $Li_2Rh_3B_2$ is formally a new structure type; however, it is closely related to the $CeCo_3B_2$ structure type [28]. The *xy* planes of both $Li_2Rh_3B_2$ and $CeCo_3B_2$ are shown in Fig. 1. $CeCo_3B_2$ crystallizes in $P6/mmm$ but it is shown in a centered orthorhombic setting ($a' = a_{hex}$; $b' = 2b_{hex}\cos 30$; $c' = c_{hex}$) to aid comparison. In both phases, the boron atoms reside at the center of a trigonal prism formed from either the rhodium or cobalt atoms. These trigonal prisms stack on top of each other in *z*, creating triangular rods, and each of these rods edge-share to form channels for the lithium or cerium cations. Both the cations and the boron atoms are at $z = \frac{1}{2}$, the rhodium atoms are at $z = 0$. In $CeCo_3B_2$, only one row of cations sit within the channel and the channel is hexagonal. In $Li_2Rh_3B_2$, there are two rows of lithium atoms within each channel and the channel distorts to accommodate them. A similar compositionally induced distortion links the compounds Li_2B_6 [29] and CaB_6 [30] that contain a topologically identical boron network. It is observed that the replacement of every calcium atom by two lithium atoms is accompanied by a symmetry-lowering distortion of the boron framework [29].

Table 3 details selected interatomic separations observed in $Li_2Rh_3B_2$; it can be seen that *c*-axis (2.8217(6) Å) defines the separation between various pairs of atoms. Fig. 2 shows the coordination geometry for the rhodium and lithium

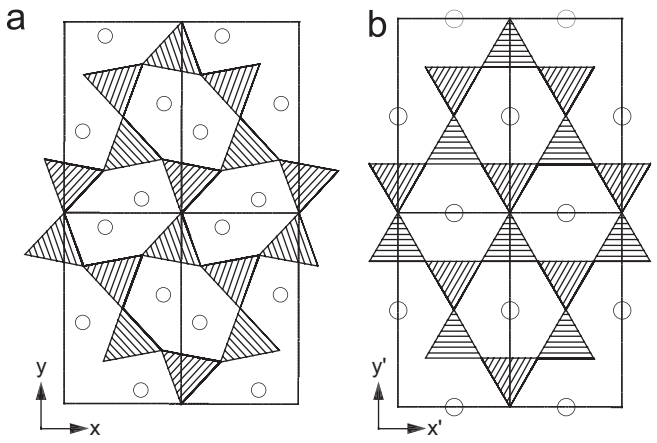

Fig. 1. The *xy* plane of (a) $Li_2Rh_3B_2$ and (b) the orthorhombic setting of the $CeCo_3B_2$ structure type. Open circles are Li or Ce; hatched triangles, Rh_6B or Co_6B trigonal prisms.

Table 3
Interatomic separations less than 3 Å

Atoms	No.	Distance (Å)	Atoms	No.	Distance (Å)
Rh(1)–Rh(1)	2	2.8217(6)	Rh(1)–B	2	2.172(4)
Rh(1)–Rh(1)	2	2.9373(6)	Rh(1)–B	2	2.191(5)
Rh(1)–Rh(2)	1	2.7908(6)	Rh(2)–B	4	2.148(4)
Rh(1)–Rh(2)	1	2.8367(6)	Li–Li	1	2.28(2)
Rh(2)–Rh(2)	2	2.8217(6)	Li–Li	2	2.8217(6)
Rh(2)–Rh(1)	2	2.7908(6)	Li–Rh(1)	2	2.601(9)
Rh(2)–Rh(1)	2	2.8376(6)	Li–Rh(1)	2	2.718(9)
Rh(1)–Li	2	2.601(9)	Li–Rh(1)	2	3.109(9)
Rh(1)–Li	2	2.718(9)	Li–Rh(2)	2	2.528(9)
Rh(1)–Li	2	3.109(9)	Li–B	1	2.49(1)
Rh(2)–Li	4	2.528(9)	Li–B	1	2.50(1)
			Li–B	1	2.79(1)

Separations of 2.8217(6) Å are defined by and parallel to the *c*-axis.

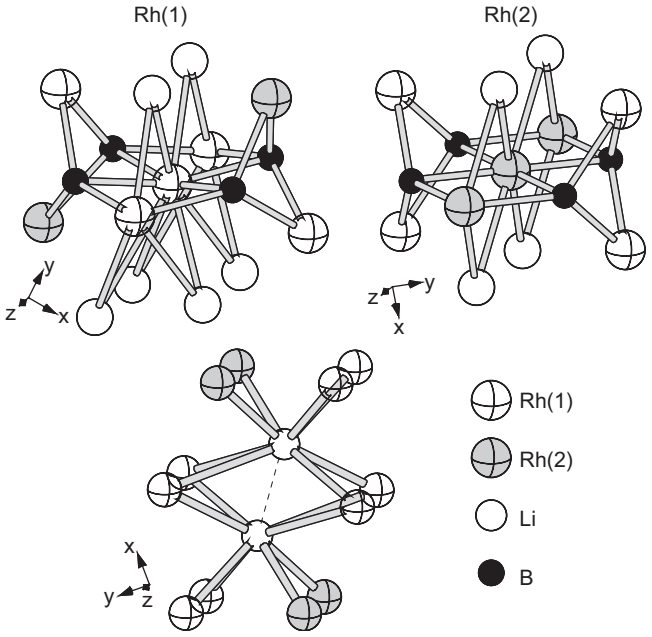

Fig. 2. The coordination environment of the rhodium and lithium atoms. The dashed line indicates the short Li–Li contact of 2.28(2) Å.

atoms; as noted above, the boron atoms are six-fold coordinate inside rhodium trigonal prisms. The Rh(1) and Rh(2) coordination environments are slightly different: both Rh(1) and Rh(2) are coordinated by six rhodium atoms (distorted octahedral) and four boron atoms (distorted square planar fashion). Rh(2) is further coordinated by four lithium atoms; in contrast, Rh(1) is coordinated by a further six lithium atoms. Rh(1) is therefore 16-coordinate and Rh(2) is 14-coordinate and, as expected, the average Rh–Li separations are shorter for Rh(2) than for Rh(1); d_{ave}[Rh(1)–Li] = 2.66 Å, d_{ave}[Rh(2)–Li] = 2.53 Å. These distances are consistent with the Li–Rh separation of 2.66 Å observed in LiRh [31]. The Rh–B and Rh–Rh separations shown in Table 2 for $Li_2Rh_3B_2$ are very similar to d(Rh–B) = 2.17, $d_{xy\text{-plane}}$(Rh–Rh) = 2.78, $d_{z\text{-axis}}$(Rh–Rh) = 2.92 Å, the equivalent separations in $CaRh_3B_2$ [32].

As shown in Table 3, there are two sets of Li–Li contacts in $Li_2Rh_3B_2$. One is defined by the *c* axis and is therefore 2.8217(6) Å, but the other is within the *ab* plane and is very short, 2.28(2) Å. Observed lithium–lithium separations range from that observed in the element, 3.03 Å, through that observed in intermetallic or Zintl phases, ~2.8 Å, to the short separation of 2.30 Å reported in the highly ionic phase Li_2O [24]. This range of Li–Li separations provides an indirect measure of the ionicity of a given lithium ion and suggests that the lithium in $Li_2Rh_3B_2$ is fully oxidized: its valence electron helps to stabilize the negatively charged, rhodium–boron covalent framework. This argument is supported by the complete lack of lithium character calculated at or below the Fermi energy (cf. "Electronic structure" section).

The $CeCo_3B_2$ structure type is common; almost all the rare earth elements and alkaline earth elements are represented in phases with the iron, cobalt and nickel group of elements. Platinum is an exception, forming compounds of the type RPt_2B (R = La, Pr, Nd [24]). According to our databases [24], $Li_2Rh_3B_2$ is the only reported material in which two columns of cations have been introduced into the channel of the $CeCo_3B_2$ structure type. However, we note that the stoichiometry $Li_2Rh_3B_2$ is mentioned in Ref. [33] and the compound reported in Ref. [16]. We attempted to replace rhodium with cobalt or iridium, but these reactions were not successful; the identifiable phases in the powder X-ray diffractograms being either a mixture of CoB and Co_2B, or LiIrB.

3.2. Electrical resistivity

The measured resistivity of a single crystal of $Li_2Rh_3B_2$ is shown in Fig. 3, no superconducting transition is observed above 2.3 K. Both the temperature dependence and the magnitude of the resistivity are consistent with metallic conduction. The data can be compared to that measured by Yamada et al. for the *c*-axis resistivity of a single crystal of $LaRh_3B_2$ ($T > 3.1$ K), where the resistivity is observed to fall from 24 to 1 μΩ cm between room temperature and 3.1 K [34]. This compares to $\rho(299\,\text{K}) = 19\,\mu\Omega\,\text{cm}$ and $\rho(2.3\,\text{K}) = 1.8\,\mu\Omega\,\text{cm}$ for $Li_2Rh_3B_2$.

3.3. Magnetic susceptibility

In addition to the data recorded on a commercial SQUID magnetometer that is presented below, all samples were screened for superconductivity to 1.3 K in a locally built SQUID magnetometer. No transitions were observed.

The observed magnetization as a function of applied field at a variety of temperatures is shown in Fig. 4 (data are uncorrected). At all temperatures measured, the sample exhibits a positive linear response at low applied field. As the applied field increases in magnitude, the sign of dM/dH changes from positive to negative and, for certain combinations of applied field and temperature, the measured magnetization is negative. The temperature

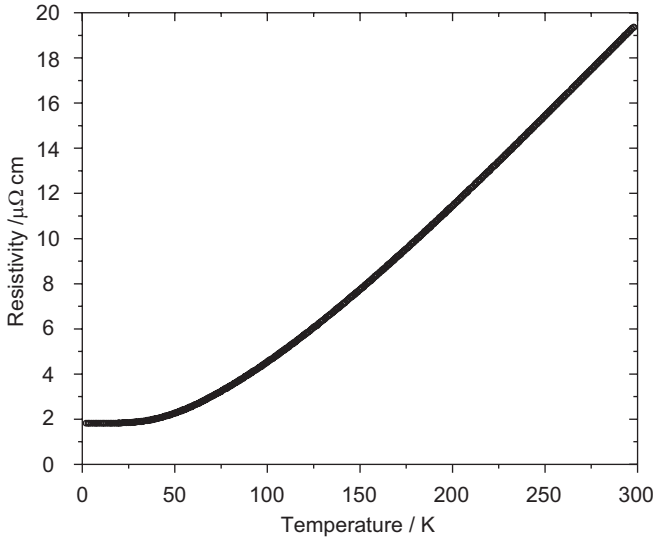

Fig. 3. The measured resistivity of a single crystal of $Li_2Rh_3B_2$.

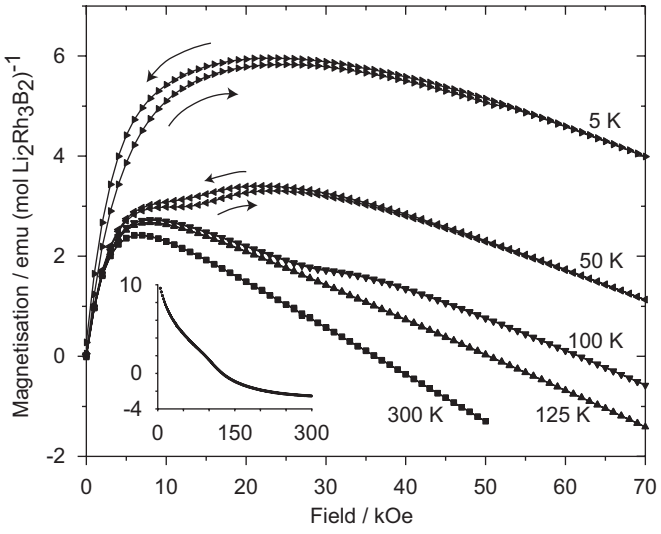

Fig. 4. The measured magnetization of a pressed pellet of $Li_2Rh_3B_2$ at various temperatures and, inset, the molar magnetic susceptibility [unit: $10^{-5}\,\text{cm}^3\,(\text{mol Li}_2\text{Rh}_3\text{B}_2)^{-1}$] as a function of temperature (unit: K) in an applied field of 50 kOe.

dependence of the magnetic susceptibility (M/H, units in figure caption) at 50 kOe is presented as an inset in Fig. 4. Consistent with the data of the main panel, the measured susceptibility is negative at higher temperatures and positive at low temperature. The overall trend of the susceptibility suggests the presence of a Curie–Weiss type paramagnetic impurity but the trend is not solely of the form $\chi_0 + C_m/(T-\Theta)$. Nevertheless, it is clear from the data that $Li_2Rh_3B_2$ is diamagnetic in the temperature range measured but that a number of impurity phases are also present in the sample puck.

The magnetization data recorded at 300 and 125 K demonstrate that the sample contains a relatively soft ferromagnetic impurity, while the data recorded at 100 and 50 K demonstrate the presence of an impurity that

undergoes a metamagnetic transition. The metamagnetic transition is pushed to lower applied field with lower temperature, being completely obscured by 5 K. The magnetic susceptibility data shown in the inset to Fig. 4 can be understood by invoking a diamagnetic majority phase, $Li_2Rh_3B_2$, a Curie–Weiss paramagnetic impurity and, consistent with the M vs. H data, a metamagnetic impurity. We note, however, that the concentration of such impurities is quite low as none was observed by powder X-ray diffraction.

In order to extract a value for the molar magnetic susceptibility, χ_{mol}, attempts were made to correct for the ferromagnetic impurity (e.g., via Owen–Honda plots [35]) and to subsequently fit the corrected high-temperature magnetic susceptibility data to $\chi_0 + C_m/(T-\Theta)$ $(T > 150\,K)$· However, due to the small magnitude of the intrinsic susceptibility of $Li_2Rh_3B_2$, a meaningful fit could not be obtained. Instead, χ_{mol} was estimated from the slope of the linear regions of the M vs. H curves (Fig. 4, main panel) at 300 K ($H \geqslant 20$ kOe), 125 K ($H \geqslant 20$ kOe) and 100 K ($H \geqslant 50$ kOe). The values so obtained were $\chi_{mol}(300\,K) = -9.3 \times 10^{-5}\,cm^3\,(mol)^{-1}$, $\chi_{mol}(125\,K) = -7.1 \times 10^{-5}\,cm^3\,(mol)^{-1}$ and $\chi_{mol}(100\,K) = -6.7 \times 10^{-5}\,cm^3\,(mol)^{-1}$. The magnitude of χ_{mol} decreases with decreasing temperature because of the Curie–Weiss type impurity present in the sample. Therefore, $\chi_{mol}(300\,K) = -9.3 \times 10^{-5}\,cm^3\,(mol)^{-1}$ is the estimate closest to the intrinsic susceptibility of $Li_2Rh_3B_2$, but this value provides only a lower limit on the magnitude of χ_{mol}. This diamagnetism contrasts with $LaRh_3B_2$, which exhibits a paramagnetic response above its superconducting transition temperature [36]. However, it is consistent with the recently reported, weakly diamagnetic phase $Mg_{1-x}RhB$ [37].

It is clear from Fig. 4 that the core diamagnetism has the largest contribution to the intrinsic susceptibility of $Li_2Rh_3B_2$. Neither lithium nor boron has sufficient electron density to account for the magnitude of χ_{mol}. We thus attribute the diamagnetism to a closed shell d^{10} configuration on rhodium, a postulate supported by electronic structure calculations below.

3.4. Electronic structure

The calculated density of states (DOS) and the projection of the boron and rhodium states are shown in Fig. 5. There is no significant lithium character in the bands at or below the Fermi energy in agreement with the highly ionic lithium–lithium separation described earlier. In both figures, there is clearly a non-zero density of states at the Fermi level and therefore the calculations predict $Li_2Rh_3B_2$ to be metallic, in agreement with the measured resistivity. The low-level states between −15 and −20 eV derive primarily from the boron s orbitals but there are strong interactions with the rhodium $5s$, $4d_{xz}$ and $4d_{yz}$ orbitals. The large peak in the DOS between −10 and −15 eV derives from the rhodium $4d$ orbitals. All these bands are below the Fermi level and are therefore filled, suggesting d^{10} rhodium atoms as supported and suggested by the measured diamagnetic susceptibility of $Li_2Rh_3B_2$. The character of the bands at the Fermi energy derives mainly from the boron and rhodium p orbitals but with a small contribution from the rhodium $4d_{z2}$, $4d_{xy}$, $4d_{x2-y2}$.

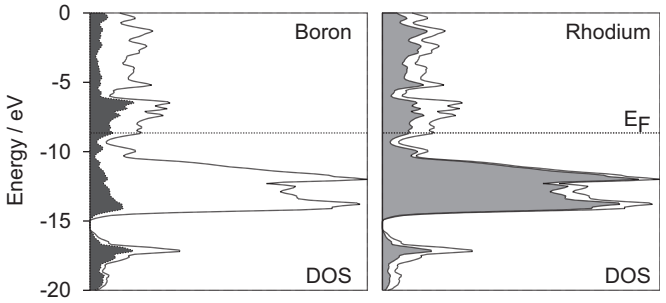

Fig. 5. The calculated density of states for $Li_2Rh_3B_2$ with either the projection of the boron or rhodium states. E_F denotes the Fermi energy and assumes 70 valence electrons per unit cell.

An interesting exercise is to assign formal charges to the atoms: it is reasonable to assume that the lithium ions are fully oxidized and the magnetic susceptibility suggests that the rhodium is d^{10}; thus, the formal charge of the boron atoms is +0.5: $(Li^{+1})_2(Rh^{-1})_3(B^{+0.5})_2$. The calculated net charges, derived from the occupation of the atomic orbitals and rounded to one decimal place, are $(Li^{+1})_2(Rh^{-0.7})_3(B^{+0.1})_2$ which, while quantitatively different from our model, do support the hypothesis of a formally negatively charged rhodium ion, suggesting that $Li_2Rh_3B_2$ is better described as a "rhodide" rather than a boride.

$LaRh_3B_2$ is paramagnetic metal that becomes superconducting below ~3 K and adopts the $CeCo_3B_2$ structure type [28]. The structure of $LaRh_3B_2$ is therefore very similar to that of $Li_2Rh_3B_2$ (see Fig. 1). The DOS of $LaRh_3B_2$, as calculated with the KKR [38] and self-consistent APW-LDA [39] method, can be compared to the calculated tight-binding DOS for $Li_2Rh_3B_2$ shown in Fig. 5. The states below the Fermi energy, i.e., those due mainly to the rhodium and boron, agree well with that calculated for $LaRh_3B_2$. According to the calculations of Takegahara et al. [39], in $LaRh_3B_2$ the character of the bands at the Fermi level is predominantly rhodium $4d$ with smaller contributions from the rhodium $5p$, boron $2p$ and the lanthanum $5d$. This contrasts with the calculations presented here for $Li_2Rh_3B_2$, where the contributions from the rhodium $4d$ states are much less significant and, of course, there is no d orbital contribution from the lithium atoms. Further differences between the DOS of $LaRh_3B_2$ and $Li_2Rh_3B_2$ occur above the Fermi level where contributions from the lanthanum $4f$ and $5d$ orbitals give rise to additional features in the calculated DOS.

It is informative to ask why $LaRh_3B_2$ superconducts below ~3 K but, according to our measurements, $Li_2Rh_3B_2$ remains metallic to 1.3 K. Three potentially important differences between $LaRh_3B_2$ and $Li_2Rh_3B_2$ are: the difference valence electron count; the structural distortion present in $Li_2Rh_3B_2$; and the difference in the character of the bands at the Fermi level/effect of the different cation.

The compound $CaRh_3B_2$ [32] is isostructural to $LaRh_3B_2$ but isoelectronic to $Li_2Rh_3B_2$ and hence provides an interesting link between the two phases. The synthesis of $CaRh_3B_2$ has been reported, but no physical properties measurements were detailed [32]. In-house magnetization measurements to 1.3 K of three different samples containing $CaRh_3B_2$ did not reveal any evidence for a superconducting transition [40]. This suggests that it is not the structural distortion of the rhodium–boron framework that is solely responsible for the lack of a superconducting transition in $Li_2Rh_3B_2$; rather, the electron count and/or the different interaction between the rhodium–boron framework and either the lanthanum or lithium cation(s) is more important.

4. Conclusions

Via the synthesis of $Li_2Rh_3B_2$, we have demonstrated that lithium is a viable medium for growing boron-containing materials. $Li_2Rh_3B_2$ exhibits diamagnetism, consistent with the calculated d^{10} configuration for rhodium, and metallic resistivity to the lowest temperatures we measured, despite its structural similarities to $LaRh_3B_2$, a material that becomes superconducting below 3 K. We speculate that an important factor determining the differing transport properties of $Li_2Rh_3B_2$ and $LaRh_3B_2$ is the nature of the interaction between the rhodium–boron framework and the lithium or lanthanum cation.

Acknowledgments

This work was supported by the US Department of Energy, Division of Basic Energy Sciences—Materials Sciences, under Contract DE-AC02-06CH11357.

References

[1] J. Nagamatsu, N. Nakagawa, T. Muranaka, Y. Zenitani, J. Akimitsu, Nature 410 (2001) 63–64.
[2] D.R. Linde (Ed.), CRC Handbook of Chemistry and Physics, 85th ed, CRC Press, Boca Raton, FL, 2004–2005, pp. 12–69.
[3] R.J. Cava, H. Takagi, B. Batlogg, H.W. Zandbergen, J.J. Krajewski, W.F. Peck Jr., R.B. van Dover, R.J. Felder, T. Siegrist, K. Mizuhashi, J.O. Lee, H. Eisaki, S.A. Carter, S. Uchida, Nature 367 (1994) 146–148.
[4] D.C. Johnston, H.F. Braun, in: M.B. Maple, Ø. Fischer (Eds.), Superconductivity in Ternary Compounds II, Springer, Heidelberg, New York, 1982, pp. 11–55.
[5] J.G. Bednorz, K.A. Müller, Z. Phys. B: Condens. Matter 64 (1986) 189–193.
[6] K. Togano, P. Badica, Y. Nakamori, S. Orimo, H. Takeya, K. Hirata, Phys. Rev. Lett. 93 (2004) 1 247004-1–247004-4.
[7] P. Badica, T. Kondo, K. Togano, J. Phys. Soc. Jpn. 74 (2005) 1014–1019.
[8] M. Wörle, R. Nesper, Angew. Chem. Int. Ed. 39 (2000) 2349–2353.
[9] P.G. Perkins, in: V.I. Matkovich (Ed.), Boron and Refractory Borides, Springer, Berlin, Heidelberg, New York, 1977, pp. 31–51.
[10] T. Lundström, in: V.I. Matkovich (Ed.), Boron and Refractory Borides, Springer, Berlin, Heidelberg, New York, 1977, pp. 351–376.
[11] U. Eibenstein, W. Jung, J. Solid State Chem. 133 (1997) 21–24.
[12] K.-W. Lee, W.E. Pickett, Phys. Rev. B 72 (2005) 174505-1–174505-8.
[13] M.G. Kanatzidis, R. Pöttgen, W. Jeitschko, Angew. Chem. Int. Ed. 44 (2005) 6996–7023.
[14] J.R. Salvador, D. Bilc, S.D. Mahanti, M.G. Kanatzidis, Angew. Chem. Int. Ed. 41 (2002) 844–846.
[15] P.C. Canfield, B.K. Cho, K.W. Dennis, Physica B 215 (1995) 337–343.
[16] R. Mirgel, Ph.D. Thesis, University of Köln, Germany, 1986.
[17] APEX2 (Version 1.22, 2004) and SAINT-Plus (Version 7.06a, 2003), Bruker Analytical Instruments, Inc., Madison, WI.
[18] G.M. Sheldrick, SADABS (Version 2.10) program for absorption correction, Bruker Analytical X-ray Instruments, Inc., Madison, WI.
[19] Sheldrick, G.M. SHELX-97, Bruker Analytical X-ray Instruments, Inc., Madison, WI.
[20] L.J. Farrugia, J. Appl. Crystallogr. 32 (1999) 837–838.
[21] H. Claus, U. Welp, H. Zheng, L. Chen, A.P. Paulikas, B.W. Veal, K.E. Gray, G.W. Crabtree, Phys. Rev. B 64 (2001) 144507-1–144507-9.
[22] G. Landrum, YAeHMOP (Version 3.0), ⟨http://yaehmop.sourceforge.net⟩.
[23] Extended Hückel parameters: Li 2*s* $H_{ii} = -5.400$ eV, $\zeta_1 = 0.6500$; Li 2*p* $H_{ii} = -3.500$ eV, $\zeta_1 = 0.6500$; B 2*s* $H_{ii} = -15.200$ eV, $\zeta_1 = 1.3000$; B 2*p* $H_{ii} = -8.500$ eV, $\zeta_1 = 1.3000$; Rh 5*s* $H_{ii} = -8.0900$ eV, $\zeta_1 = 2.1350$; Rh 5*p* $H_{ii} = -4.5700$ eV, $\zeta_1 = 2.1000$; Rh 4*d* $H_{ii} = -12.500$ eV, $\zeta_1 = 4.2900$, $c_1 = 0.6860$, $\zeta_2 = 1.9700$, $c_2 = 0.5685$.
[24] FIZ/NIST Inorganic Crystal Structure Database (Version 2005-2), ICDD Powder Diffraction File (PDF4+2006 RDB).
[25] L.M. Gelato, E. Parthé, J. Appl. Crystallogr. 20 (1987) 139–143.
[26] All units $Å^2 \times 10^3$: Rh(1), $U_{11} = 2(1)$, $U_{22} = 3(1)$, $U_{33} = 4(1)$, $U_{23} = 0$, $U_{13} = 0$, $U_{12} = 0(1)$; Rh(2), $U_{11} = 3(1)$, $U_{22} = 2(1)$, $U_{33} = 4(1)$, $U_{23} = 0$, $U_{13} = 0$, $U_{12} = 0(1)$.
[27] J. Rodríguez-Carvajal, FULLPROF version January 2006, ILL (unpublished).
[28] Yu.B. Kuzma, P.I. Kripyakevich, N.S. Bilonizhko, Dopov. Akad. Nauk. Ukr. RSR Ser. A 31 (1969) 939–941.
[29] G. Mair, H.G. von Schnering, M. Wörle, R. Nesper, Z. Anorg. Allg. Chem. 625 (1999) 1207–1211.
[30] M. von Stackelberg, F. Neumann, Z. Phys. Chem. B 19 (1932) 314–320.
[31] S.S. Sidhu, K.D. Anderson, D.D. Zauberis, Acta Crystallogr. 18 (1965) 906–907.
[32] W. Jung, J. Less-Common Met. 97 (1984) 253–263.
[33] R. Mirgel, W. Jung, J. Less-Common Met. 144 (1988) 87–99.
[34] M. Yamada, Y. Obiraki, T. Okubo, T. Shiromoto, Y. Kida, M. Shiimoto, H. Kohara, T. Yamamoto, D. Honda, A. Galatanu, Y. Haga, T. Takeuchi, K. Sugiyama, R. Settai, K. Kindo, S.K. Dhar, H. Harima, Y. Onuki, J. Phys. Soc. Jpn. 73 (2004) 2266–2275.
[35] P.W. Selwood, Magnetochemistry, second ed, Interscience, New York, 1956, pp. 351–352.
[36] Y. Kishimoto, Y. Kawasaki, T. Ohno, J. Phys. Soc. Jpn. 73 (2004) 1970–1981.
[37] A.M. Alekseeva, A.M. Abakumov, A. Leithe-Jasper, W. Schnelle, Yu. Prots, J. Hadermann, G. Van Tendeloo, E.V. Antipov, Yu. Grin, Z. Anorg. Allg. Chem. 631 (2005) 1047–1054.
[38] D.K. Misemer, S. Auluck, S.I. Kobayasi, B.N. Harmon, Solid State Commun. 52 (1984) 955–959.
[39] K. Takegahara, H. Harima, T. Kasuya, J. Phys. Soc. Jpn. 54 (1985) 4743–4751.
[40] The majority of the peaks in all three of the powder X-ray diffraction patterns of the samples could be matched to the PDF card of $CaRh_3B_2$. However, second phases such as RhB and Rh_7B_3 were always present in concentrations of up to 15%, as judged by visual inspections of the intensity of the peaks. Furthermore, mass analyses showed that arc-welding the samples led to more than just the calcium excess being lost and it is possible that the $CaRh_3B_2$ we made is calcium deficient.